Remote Sensing of Environment 192 (2017) 139–149

Contents lists available at ScienceDirect

Remote Sensing of Environment

journal homepage: www.elsevier.com/locate/rse

Global cross-calibration of Landsat spectral mixture models

Daniel Sousa *, Christopher Small

Lamont-Doherty Earth Observatory, Columbia University, Palisades, NY 10964, USA

ARTICLE INFO

Article history:
Received 30 August 2016
Received in revised form 5 January 2017
Accepted 27 January 2017
Available online xxxx

Keywords:
Landsat
Cross-calibration
Spectral mixing
Global

ABSTRACT

Data continuity for the Landsat program relies on accurate cross-calibration among sensors. The Landsat 8 Operational Land Imager (OLI) has been shown to exhibit superior performance to the sensors on Landsats 4–7 with respect to radiometric calibration, signal to noise, and geolocation. However, improvements to the positioning of the spectral response functions on the OLI have resulted in known biases for commonly used spectral indices because the new band responses integrate absorption features differently from previous Landsat sensors. The objective of this analysis is to quantify the impact of these changes on linear spectral mixture models that use imagery collected by different Landsat sensors. The 2013 underflight of Landsat 7 and Landsat 8 provides an opportunity to cross calibrate the spectral mixing spaces of the ETM+ and OLI sensors using near-simultaneous acquisitions of radiance measurements from a wide variety of land cover types worldwide. We use 80,910,343 pairs of OLI and ETM+ spectra to characterize the Landsat 8 OLI spectral mixing space and perform a cross-calibration with Landsat 7 ETM+. This new global collection of Landsat spectra spans a greater spectral diversity than those used in prior studies and the resulting Substrate, Vegetation, and Dark (SVD) spectral endmembers (EMs) supplant prior global Landsat EMs. We find only minor ($-0.01 < \mu < 0.01$) differences between SVD fractions for coregistered pairs of spectra unmixed using the new sensor-specific endmembers identified in this analysis. Root mean square (RMS) misfit fractions are also shown to be small (<98% of pixels with <5% RMS), in accord with previous studies using standardized global endmembers. Finally, vegetation is used as an example to illustrate the empirical and theoretical relationship between commonly used spectral indices and subpixel fractions. We include the new global ETM+ and OLI EMs as Supplementary Materials. SVD fractions unmixed using global EMs thus provide easily computable, linearly scalable, physically based measures of subpixel land cover area which can be compared accurately across the entire Landsat 4–8 archive without introducing any additional cross-sensor corrections.

1. Introduction

The Landsat program provides the longest continuous record of satellite imaging of the Earth available to the scientific community (Wulder et al., 2016). One great strength of this record lies in data continuity provided by the generally excellent cross-calibration between the sensors on board the different satellites (Markham and Helder, 2012). To extend this continuity into the future, the Operational Land Imager (OLI) onboard Landsat 8 must be intercalibrated with the rest of the archive. Over the 3+ years since launch, the OLI has been shown to exhibit superior performance to previous Landsat sensors with respect to radiometric calibration (Mishra et al., 2016; Morfitt et al., 2015), signal to noise (Knight and Kvaran, 2014; Morfitt et al., 2015; Schott et al., 2016), and geolocation (Storey et al., 2014).

One of the applications enabled by such a deep archive of high quality Earth observation data is multitemporal analysis to study long-baseline changes (Vogelmann et al., 2016). However, concern has recently emerged over the direct intermixing of data collected by both the OLI and older TM/ETM+ instruments onboard Landsats 4–7 because of the changes in band placement introduced with Landsat 8 (Holden and Woodcock, 2016). Statistical corrections and corresponding transfer functions have been introduced to correct for these differences (Roy et al., 2016). Considerable work has been done to examine the effect of these discrepancies and corrections in the context of spectral indices. The implications of these changes for spectral mixture analysis (SMA) are different than for spectral indices. The implications for multi-sensor and multi-temporal SMA have been investigated on the regional scale by (Flood, 2014), but, to our knowledge, no attempt has been made to address these implications for globally standardized spectral mixture models.

The purpose of this study is to characterize the global Landsat 8 OLI spectral mixing space and cross-calibrate it with the Landsat 4–7 TM/ETM+ spectral mixing space. Previous work has shown the TM and ETM+ sensors to provide globally consistent results for Substrate, Vegetation, and Dark (SVD) subpixel fraction estimates using SMA (Small, 2004; Small and Milesi, 2013). Extending this cross-calibration to

* Corresponding author.
E-mail address: d.sousa@columbia.edu (D. Sousa).

http://dx.doi.org/10.1016/j.rse.2017.01.033
0034-4257/

include imagery from the OLI onboard Landsat 8 could thus extend this consistency across the entire 30+ year archive of Landsat 4–8 imagery. In order to develop a cross calibration suitable for multi-sensor SMA, it is necessary to compare spectral mixing spaces for both sensors and identify comparable spectral endmembers that span both spaces. Under ideal circumstances, this would require spectrally diverse collections of TM/ETM+ and OLI spectra where both sensors image the same targets simultaneously.

Before Landsat 8 was placed into its final orbit, it was maneuvered into underflight configuration below Landsat 7 for one day: March 30 (Julian Day 89) 2013. While the two satellites were positioned in this way, they imaged a diversity of land cover spanning a wide range of spectral reflectance signatures. Each pair of ETM+/OLI images was collected approximately 2–5 min apart. The short temporal baseline between image pairs minimizes changes in solar illumination, surface processes and atmospheric effects. The underflight imagery thus provides a rare, nearly ideal opportunity for cross-calibration of the OLI and ETM+ sensors.

However, while the underflight dataset is nearly ideal for this purpose in many ways, there are some caveats. Standard LaSRC surface reflectance is not available for the OLI underflight data, so this analysis is limited to exoatmospheric reflectance with no atmospheric correction attempted. Furthermore, this analysis is both retrospective and global in extent, limiting the results of this study to that of an intercomparison and cross-calibration, but not a full field validation. We suggest that the unique, near-synchronous imaging geometry of the underflight data provides valuable information that is worth exploring despite these limitations.

In this study, we use 80,910,343 unsaturated broadband spectra imaged nearly simultaneously by Landsat 7 and Landsat 8 while flown in underflight configuration to address the following question: How reliably can subpixel Substrate, Vegetation and Dark (SVD) fractions be used interchangeably between ETM+ and OLI?

We find that the subscenes chosen for this analysis span an even greater range of the Landsat spectral mixing space than previous (Small, 2004; Small and Milesi, 2013) studies. We suggest that endmembers (EMs) generated for this study can thus effectively replace previous global EMs. While the new Dark (D) EM does not differ substantially from previous EMs, small differences in the Vegetation (V) EM and larger differences in the Substrate (S) EM are apparent. The overall behavior of the model is consistent with the findings of (Flood, 2014). The differences in the Vegetation EM are consistent with the findings of (Holden and Woodcock, 2016; Roy et al., 2016) as being a result of band placement. The differences in the Substrate EM are likely due to the wider range of global substrates present in this study than in any previous global study and constitute an improvement upon previous global models.

As a result, we find that subpixel estimates of SVD fractions for Landsat 8 using the old and new EMs display strong linear relations, with estimates of subpixel V fraction essentially unchanged and with easily correctible biases for S and D. When compared with the new EMs, all three SVD fractions scale linearly between the sensors with minimal ($\mu = -0.01$ to 0.01) bias. Root-mean-square (RMS) misfit to the SVD model for both the old and the new EMs is generally small, with >98% of all pixels showing <5% error.

Finally, we use vegetation as an example to show the relationship between commonly used spectral indices and subpixel EM fractions produced by SMA of Landsat 8. We suggest that fractions estimated by SMA from global EMs provide easily computable, linearly scalable, physically based measures of subpixel land cover which can be compared accurately across the entire Landsat 4–8 archive without introducing any additional cross-sensor corrections.

2. Background

a. *Implications of spectral band positioning*

The spectral response function of a sensor quantitatively defines its sensitivity to different wavelengths of light. The radiometric design of the Landsat 8 OLI featured an improvement on the previous TM/ETM+ sensors by modifying its spectral response function to narrow and slightly relocate several of the spectral bands. This has the effect of reducing the impact of common atmospheric absorptions which impede imaging the land surface (Mishra et al., 2016). However, it also has the effect of subtly changing the broadband spectrum imaged by OLI for any object which is not spectrally flat over the wavelengths for which the spectral response function was modified.

Fig. 1 shows the effect of the different spectral responses of the OLI and ETM+ sensors. Four sample green vegetation spectra (column 1) are shown, as well as four sample mineral spectra (column 3) from the USGS spectral library. The response functions of the two Landsat sensors are plotted as well to demonstrate the portions of the spectrum over which they are sensitive. The narrowing and slight adjustment to the position of the NIR and SWIR bands (black, cyan, and gold) are evident. Superimposed on each of these spectra are simulated Landsat 7 and 8 broadband spectra computed by convolving the reflectance spectra with the response functions of the sensors as described above.

Column 2 shows the difference between the OLI and ETM+ reflectances derived from the laboratory spectra. The essential shape and fundamental characteristics of the spectra are all very similar, but perceptible differences in the spectra are detectible. While the differences in aggregate are generally <0.01 reflectance units (<5%), the differences can approach 0.02 reflectance units (10%) for individual bands in some cases.

b. *Spectral mixture models and linear spectral unmixing*

At the scale of the 30 m Landsat pixel, most landscapes are spectrally heterogeneous. As a result, most pixels imaged by Landsat sensors are spectral mixtures of different materials (e.g. soils, vegetation, water, etc) with varying amounts of subpixel shadow. The continuum of aggregate radiance spectra imaged by a sensor forms a spectral mixing space in which each pixel occupies a location determined by the relative abundance of material reflectances imaged in the Ground Instantaneous Field Of View (GIFOV) of the pixel. In situations where multiple scattering among subpixel targets is small compared to single scattering from each subpixel target to the sensor, the aggregate response of the sensor often varies in proportion to the relative abundance of the spectrally distinct materials (Singer and McCord, 1979).

The topology of the full space of radiance (or equivalently reflectance) spectra reveals the linearity of mixing and the composition of the spectral endmembers and mixtures that bound the space of all other observed spectral mixtures (Boardman, 1993). In the case of decameter resolution sensors like those on the Landsat satellites, the combination of spatial and spectral resolution, and positioning of the spectral bands, resolves characteristics of reflectance spectra that distinguish the most spectrally distinct materials commonly found in landscapes. Ice, snow, rock and soil substrates, vegetation, and water each represent a general class of reflectance spectra that are clearly distinguishable with broadband sensors at decameter spatial scales (Small, 2004). Of these, the aggregate broadband reflectances of most landscapes can be represented accurately as linear mixtures of substrate (S), vegetation (V) and dark (D) endmembers. The dark endmember corresponds to either absorptive, transmissive or non-illuminated surfaces and typically represents either shadow or water. As a result, linear combinations of these three spectral endmembers can represent the aggregate reflectance of a very wide range of landscapes at meter to decameter scales (Small and Milesi, 2013).

By identifying the SVD endmember spectra that bound the spectral mixing space, it is possible to use these endmembers together with a linear spectral mixture model to project the 6D feature space of the Landsat sensors onto a simpler 3D mixing space bounded by spectrally and functionally distinct components of a wide range of landscapes (Adams et al., 1986). Inverting a simple three endmember linear spectral mixture model using the SVD endmembers yields estimates of

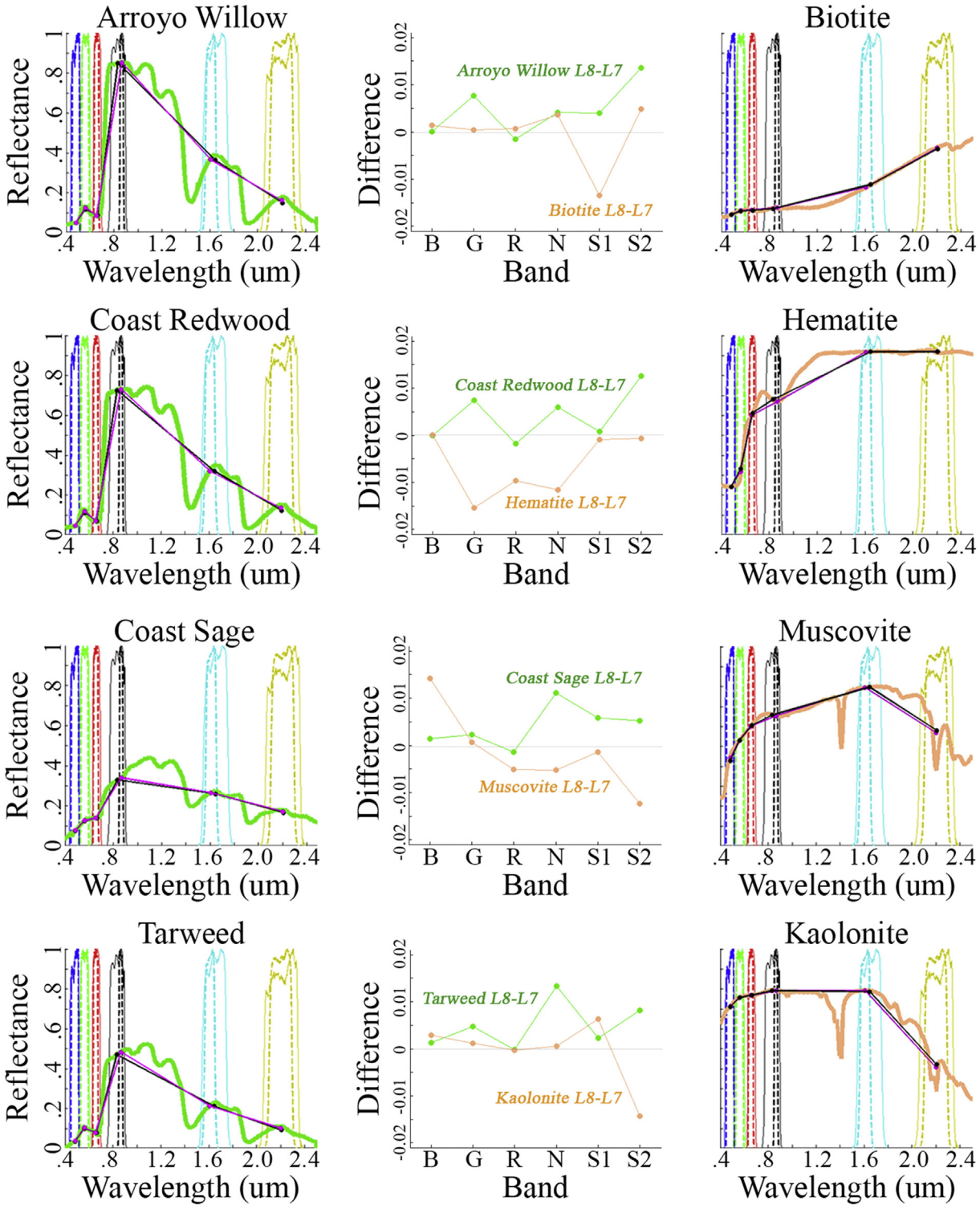

Fig. 1. Illustration of the effect of changes in spectral response functions for Landsat 8 OLI and Landsat 7 ETM+. Laboratory spectra from the USGS spectral library for sample vegetation (column 1) and minerals (column 3) convolved with the spectral response functions of OLI and ETM+. The simulated reflectance for each sensor is shown in thick lines (L7 = black, L8 = magenta). The spectral response functions are generally wider for ETM+ (solid thin lines) than OLI (dashed lines). Differences in broadband reflectance as observed by ETM+ and OLI (center) depend on both overall albedo and on the depth, width and location of absorptions. While both sensors record similar spectra, individual band-to-band differences can be nearly 0.02 reflectance units, sometimes exceeding 10% of the value of an individual band. (For interpretation of the references to colour in this figure legend, the reader is referred to the web version of this article.)

areal abundance of each endmember for each pixel in an image. Using standardized spectral endmembers that span the global mixing space of spectra allows for intercomparison of fraction estimates derived from different sensors across space and time. Standardized spectral endmembers confer all of the benefits of spectral indices, with the added benefit of using all of the spectral information available while simultaneously representing multiple spectral contributions to the mixed pixel.

c. *Scientific context and limitations of the study*

The approach taken in this paper is to calibrate global spectral mixture models of Landsat ETM+ and OLI imagery using the novel global collection acquired during the Landsat 7 and 8 underflight. While this has not previously been accomplished, a regional study in Australia examining the continuity of ETM+ and OLI performance in a multiple linear regression model, a spectral mixture model, and a spectral index was performed by (Flood, 2014). In the analysis of (Flood, 2014), the problem is approached in a different way: ETM+ and OLI imagery from subsequent overpasses (8 days apart) were bias corrected band-by-band before being input into biophysical models. Orthogonal Distance Regression was used to cross-calibrate the imagery, which was then used to a) predict overstorey foliage projective cover, (an areal estimate of vegetation), using top of atmosphere (TOA) reflectance; b) predict fractional vegetation cover with a linear mixture model of bare soil, photosynthetic, and non-photosynthetic vegetation, using modeled surface reflectance; and c) compute NDVI. Large systematic changes were reported in the Near Infrared and Shortwave Infrared 2 bands, with surprisingly little change in the Shortwave Infrared 1 band. The approach of (Flood, 2014) corrected for these differences well, resulting in regression slopes equal to 1.00 and good agreement between ETM+ and OLI fractional land cover.

The collection of Landsat 7/8 underflight data undersamples the surface of the Earth in both space and time. Notably, there are unfortunately no cloud-free acquisitions over dense tropical forests. The season of the overpass (late March) results in imaging of senescence of many high latitude boreal forests. However, this is unlikely to result in appreciable variability in either the vegetation or dark EMs because, as shown previously (Small and Milesi, 2013), these two EMs show negligible change on a global scale when compared even with the limited global subset of (Small, 2004). That the ETM+ vegetation and dark EMs from this study are very similar to those found by the two previous studies mentioned here is further evidence that undersampling of vegetation and dark EMs is not an appreciable source of uncertainty in this analysis.

However, representation of an unusually diverse subset of the global substrates is a strength of this collection. The global plane of substrates has previously been shown to be spectrally diverse. Greater sampling of this portion of the space than was achieved in previous studies further supports the linear mixing hypothesis in the substrate-rich (and vegetation-sparse) region of the mixing space, and yields a new global substrate EM which provides the most complete bound on the global Landsat mixing space to date.

This study is performed with TOA reflectance in order to provide a direct comparison with previous studies and to minimize the complexity of the analysis. As mentioned in the introduction, standard LaSRC surface reflectance processing is not available for pre-WRS2 Landsat 8 data (USGS, 2016), and modeling of surface reflectance was not attempted. Furthermore, the retrospective nature of the study precludes true field validation. The global extent of the study and the remote location of many of the subscenes precludes precise knowledge of atmospheric or BRDF parameters at the time of the overpass.

The clear atmospheric conditions present in the subscenes we chose for the analysis was fortuitous and minimizes the contamination by atmospheric effects that is common in satellite imaging. Mixture models cannot correct for most atmospheric contamination problems and surface reflectance should be used whenever well constrained atmospheric corrections are available.

The unique nature of the near-simultaneous acquisitions in the underflight dataset greatly reduces the problems of imaging geometry and atmospheric change which surface reflectance is designed to overcome. The level of mixture model agreement given by TOA reflectance in this study allows us to take a conservative stance on the level of data preprocessing. We do this in order to avoid introducing unnecessary sources of uncertainty that can result from using an unjustifiably complex model. However, a similar analysis characterizing the global Landsat mixing space with modeled surface reflectance and field validation would be a valuable line of inquiry in the future.

3. Data & methods

All data used in this study were acquired from the USGS Earth Resources Observation and Science Center at http://glovis.usgs.gov/. Landsat 8 data were acquired from the "Landsat 8 OLI Pre-WRS 2" collection. Data were processed from DN to radiance (L) using the following expression:

$$L_\lambda = \text{Gain} * \text{DN} + \text{Bias}$$

Exoatmospheric reflectance (Chander and Markham, 2003) was then computed using the following expression:

$$\rho_\lambda = \frac{\pi L_\lambda d^2}{\text{ESUN}_\lambda \sin\theta}$$

where ρ_λ is the reflectance at a given wavelength, d is the earth-sun distance, $ESUN_\lambda$ is the solar irradiance, and θ is the sun elevation in degrees. We manually selected a set of 100 30 × 30 km subscenes from the spatial overlap between the Landsat 7 and 8 acquisitions on the basis of maximum spectral diversity. Nearly all of the subscenes were cloud-free, although some subscenes which contained land cover with unusually diverse spectral properties were included even if minor cloud contamination was present. Both Landsat 7 and 8 analyses were performed only on pixels unaffected by the SLC-off gaps. No saturated pixels were used in this analysis.

Linear spectral unmixing represents each pixel reflectance factor (R) as a linear combination of the input spectral EMs (M) weighted by their areal fractions (f) plus misfit (ε) as $R = fM + \varepsilon$. A unit sum constraint is often used, which amounts to adding an additional equation that the fraction estimates sum to unity ($\Sigma f = 1$). This set of equations is overdetermined and the coefficients for the optimal linear combination of EMs to represent each pixel under the L2 norm can be directly computed using Weighted Least Squares, where the relative weight of the unit sum constraint is a tunable parameter. All unmixing was performed with unit sum constraints with weight = 1.

4. Analysis

Fig. 2 shows the locations of the 30 Landsat 7 and 8 scene pairs used in this analysis. All scene pairs were collected in underflight configuration. The time difference between Landsat 7 and 8 overpasses was <6 min for every scene pair. The scenes span a remarkable geographic diversity of land cover given the short time in which they were collected. Five continents are represented. Although several images were acquired over mainland Europe (Path 198), unfortunately all except the one covering Ibiza, Spain were too cloudy for the purposes of this analysis.

From these 30 image pairs, 100 subscenes of 1,000,000 spectra each were chosen on the basis of spectral diversity (Fig. 3). Subscenes are shown both with a common linear stretch (TOA reflectance = 0 to 0.7) and subscene specific 2% linear stretches in an attempt to show the spectral diversity and complexity included in this sample. Shallow and deep water are each represented in both coastal and inland water bodies. Natural and managed vegetation are both present over a wide range of climate zones and soil types. Geologic diversity includes both mafic and felsic bedrock, Quaternary alluvium, and sand dunes with variable grain size and lithology. One large evaporite pan near Kuwala, India was included to demonstrate the performance of spectrally complex minerals in the global SVD model. Despite several cloud-free acquisitions at high northern latitudes, snow and ice was minimized due to its minor areal coverage within the terrestrial ecoregions of the world

Fig. 2. Locations of 30 near-simultaneous Landsat 7/8 scene pairs from which the 100 subscenes for this analysis were chosen. For every scene pair, Landsat 7 and Landsat 8 overpass times were within 6 min of each other. All scenes were imaged while Landsat 8 was performing its pre-WRS2 underflight of Landsat 7 on March 30 (JD 89), 2013.

(Olson et al., 2001) and the fact that a larger sample would be required to accurately represent its true spectral diversity. When pixels in the SLC-off gaps of Landsat 7 are removed, a total of 80,910,343 coregistered ETM+ and OLI spectra remain.

Principal Component (PC) analysis was then performed independently on both the Landsat 7 and Landsat 8 subscene mosaics. Landsat 8 Coastal/Aerosol and Cirrus bands were not included in the analysis in order to facilitate a direct comparison between the sensors. The resulting Landsat 8 spectral mixing space with corresponding single pixel EMs is shown in Fig. 4. The Landsat 7 mixing space is not shown, as it is visually indistinguishable from the Landsat 8 space. As found in previous work, the space is characterized by sharp, clear apexes corresponding to Vegetation and Dark EMs, but substantial complexity near the Substrate EM. This complexity reflects the diverse range of rocks and soils spanning the plane of substrates. Sharp linear edges connecting (D,V) and (D,S) EMs (clearly visible in the projection showing PC 1 and PC 3) indicates binary linear mixing. Concavity on the edge connecting (S,V) suggests that Substrate and Vegetation rarely trade off completely without any subpixel shadow. The elongate cluster of pixels spectrally distinct from the global mixing space corresponds to the Evaporite pan (E) in India. The inclusion of these evaporites allows an opportunity to illustrate the behavior of the model to materials which are not linear combinations of substrate, vegetation, or dark targets in broadband visible-IR spectra. Inclusion of these evaporites in the PC rotation does not affect the other fractions because EMs were manually chosen from the other apexes of the space.

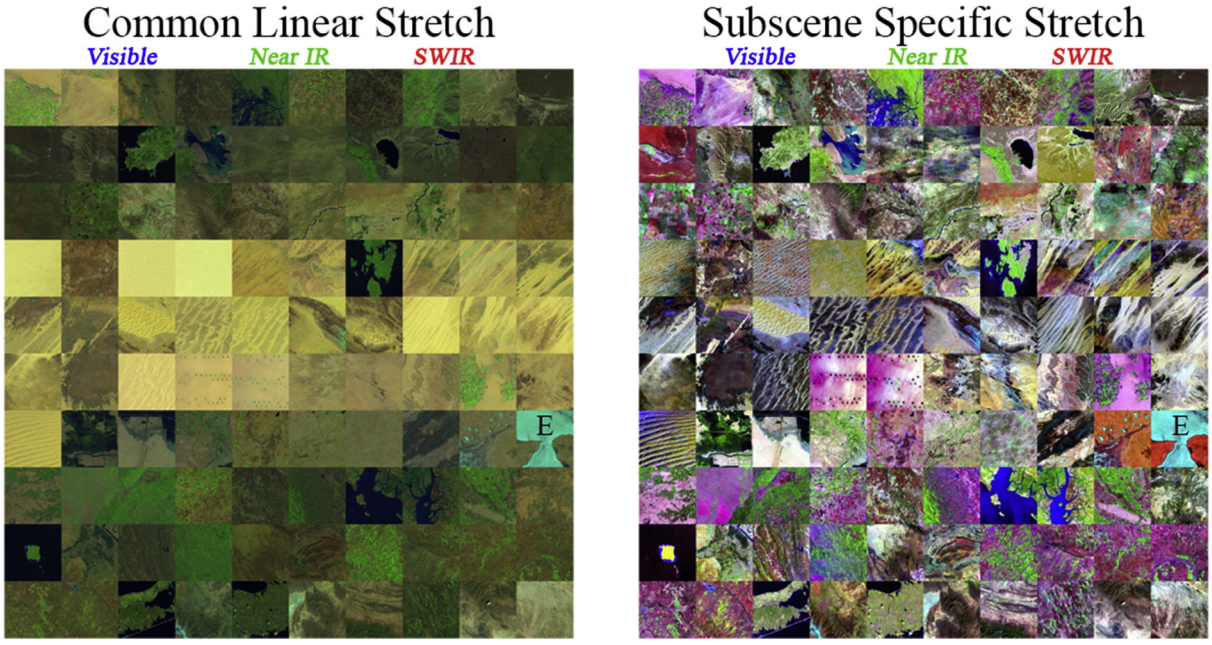

Fig. 3. Comparison of 100 OLI subscenes chosen from the near-simultaneous Landsat 7 and Landsat 8 acquisitions from Fig. 2. Each 30 × 30 km subscene is shown with both a common linear stretch (reflectance = 0 to 0.7) as well as with subscene-specific 2% linear stretches to illustrate the spectral diversity of the scenes chosen. The subscenes sample a range of evergreen and deciduous natural vegetation, agriculture, lithologically variable soil, sediment, and rock substrates, as well as standing water (both deep and shallow). With the exception of the evaporite pan in western India (labeled E), all subscenes are composed of varying mixtures of rock and soil substrates, vegetation, water and shadow.

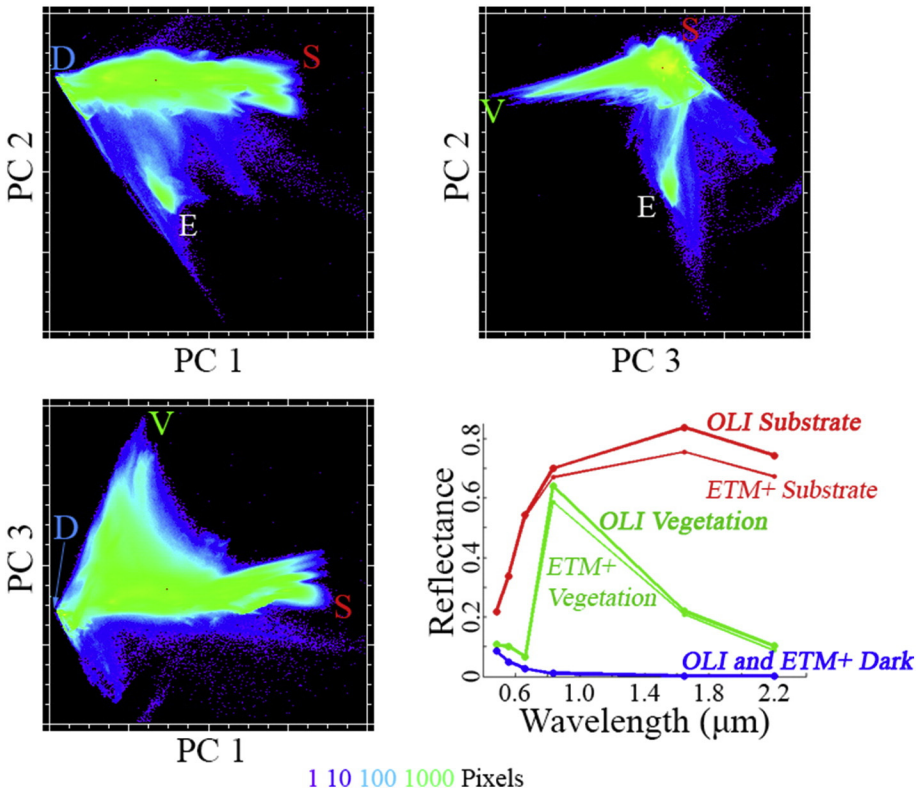

Fig. 4. The Landsat 8 OLI spectral mixing space derived from 80,910,343 broadband spectra. The Landsat 7 ETM+ mixing space (not shown) of the near-simultaneous Landsat 7 acquisitions is visually indistinguishable. EM spectra (lower right) selected from the apexes of the scatterplot correspond to the same geographic locations so represent the same materials - within the uncertainty in the coregistration of each OLI/ETM+ image pair. The prominent cluster with distinct PC 2 values (E) corresponds to an evaporite pan near Kuwala, India. (For interpretation of the references to colour in this figure, the reader is referred to the web version of this article.)

Substrate (red), Vegetation (green) and Dark (blue) global EM spectra are shown in Fig. 4. The differences between the ETM+ and OLI EM spectra are a result of the changes in spectral response functions between the sensors. These pairs of spectra represent identical geographical locations imaged at nearly the same time. The Substrate EM corresponds to a field of sand dunes in the Libyan Sahara (p184r044), the Vegetation EM corresponds to a homogenous agricultural field in central Texas (p029r038), and the Dark EM corresponds to deep water off the Atlantic coast of Long Island, New York (p013r032). While the dark EM is nearly identical for the two sensors, the Landsat 8 substrate and vegetation EMs are brighter than the Landsat 7 EMs in all IR wavelengths, most prominently in the NIR and SWIR 1. Text files with EM spectra for both ETM+ and OLI sensors are included as Supplementary materials.

As expected, the geometry of the mixing space shown here, as well as the ETM+ spectra of the resulting Vegetation and Dark EMs, are similar to those found by previous studies (RMS differences with (Small and Milesi, 2013) of 0.02 and 0.00 for V and D, respectively). However, the Substrate EM is substantially brighter across all wavelengths than found previously (RMS differences with (Small and Milesi, 2013) of 0.14 for the new OLI EM and 0.10 for the new ETM+ EM). The plane of substrates found in this study is inclusive of the spectral range found by prior studies, but also contains substantially greater variability in bright sands. This extension of the plane of substrates is likely a result of the range of diversity of sands and soils included in this analysis. The newly identified substrates represent an improvement over previous models as they are more general and inclusive of the range of landscapes present on the surface of the Earth.

The newly identified global EMs were used to unmix the collections of both OLI and ETM+ underflight spectra. Fig. 5 shows the comparison of SVD fraction estimates from Landsat 8 OLI spectra as unmixed using the previous (Small and Milesi, 2013) global EMs and the new underflight OLI EMs. As expected given the new, more reflective substrate EM, substrate fractions are substantially lower and dark fractions are substantially higher with the new EMs than with the old. Note that the x-axes of the Substrate and Dark plots are truncated at upper bounds of 1.2 and lower bounds of −0.2, respectively. A substantial number of pixels have substrate fractions as high as 1.4 and dark fractions as low as −0.4 when unmixed with the old EMs. This is expected as a result of the significantly higher SWIR reflectance of the new OLI substrate EM. The new EMs more effectively span the global mixing space and result in the physically plausible bounds of 1.0 and 0.0 for these fractions. By extending the apexes of the Substrate and (to a lesser degree) Vegetation EMs, the new OLI & ETM+ mixing spaces encompass the earlier mixing spaces bounded by the older EMs.

The vegetation fractions in Fig. 5 plot close to the 1:1 line, indicating that vegetation estimates are essentially unchanged between the old and new sets of EMs. RMS error magnitudes are essentially unchanged between the two sets of EMs, with >98% of all pixels showing error < 5%. As expected, the evaporites plot distinctly off the 1:1 line for all fractions, showing reduced S, increased V, and reduced D fractions relative to the rest of the global space. These values are clearly erroneous and reflect the inability of the SVD model to represent evaporite reflectance accurately. The evaporite EM is not included in the SVD model because evaporites represent a small fraction of Earth's surface and lie outside the primary SVD hull that represents most landscapes. However, the quasi-linear binary mixing trend between the evaporite and dark EMs suggests that a linear mixture model might be useful for mapping variations in moisture content of evaporites. We do not include an evaporite EM here because our single acquisition is not necessarily representative of the true diversity of evaporites and range of moisture contents. We omit ice and snow EMs for the same reason.

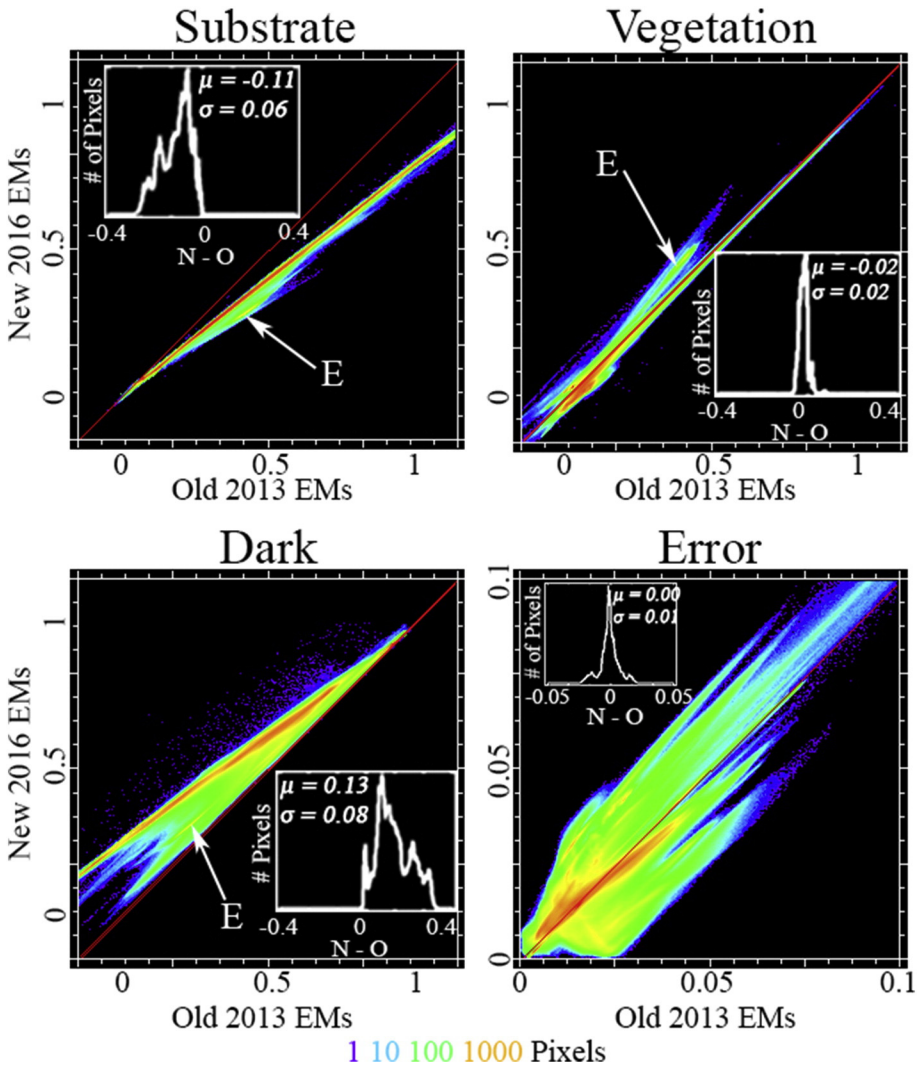

Fig. 5. SVD fraction intercomparison for 80,910,343 Landsat 8 spectra by unmixing with old (Small and Milesi, 2013) global EMs and the new 2016 EMs. OLI fractions unmixed with both sets of EMs are strongly linear - even though the EMs were derived from independent global collections of spectra. Unmixing with old EMs shows a clear bias toward higher substrate fractions ($\mu = -0.11$) and lower dark fractions ($\mu = 0.13$) than using the new EMs. Vegetation fraction shows a small bias ($\mu = -0.02$). Error fractions are slightly lower for the new EMs than the old EMs, but >98% of all pixels have error < 5% for both models. The cluster of pixels distinctly plotting off the linear S, V, and D relations corresponds to evaporites (E) which are not well represented by either simple 3 EM model. Histogram insets show fraction difference (New - Old) between the two models.

Fig. 6 shows the cross comparison between Landsat 8 underflight fractions unmixed using the new OLI global EMs (thick lines from Fig. 4) and Landsat 7 underflight fractions unmixed using the corresponding new global ETM+ EMs (thin lines from Fig. 4). Biases for all fractions are small ($-0.01 < \mu < 0.01$) and all fractions cluster tightly around the 1:1 line ($\sigma = 0.03$ for all fractions and $\sigma = 0.00$ for error). The small number of pixels plotting substantially off the 1:1 line can generally be visually identified as either: 1) movement of macroscale clouds, 2) microscale atmospheric parameters such as aerosol or water vapor content which changed over the 1–6 min between satellite overpasses or 3) land cover types poorly fit by the global SVD model such as snow/ice or shallow/turbid water. The evaporite cluster remains clearly distinct as a reminder of the limits of the model. Some of the dispersion about the 1:1 line may also be attributed to spatial misregistration between Landsat 7 and 8, although visual comparison shows qualitatively excellent coregistration in most cases. This suggests that subpixel displacements between the Landsat 7 and Landsat 8 acquisitions may introduce fraction differences of several percent in some cases, although the majority of pixels agree to well within 3%. Pixels from the evaporite pan are included in the calculation of the descriptive statistics listed here. Exclusion of the evaporite pan would result in a minor reduction in the bias, dispersion, and overall RMS misfit reported here. We choose to include the evaporites in our statistics in order to provide a more conservative estimate of the power of the model on a global scale. The linearity, lack of bias, and tight clustering of these scatterplots suggest TM/ETM+ and OLI imagery can be safely used interchangeably when unmixed using these global EMs. Although subtraction of the fraction bias values given here might improve agreement between TM/ETM+ and OLI fractions, the bias in each case is significantly smaller than the 0.03 to 0.07 fraction estimate uncertainty found in vicarious validations of Landsat SVD fractions with aggregated SVD fractions from near simultaneous WorldView2 acquisitions (Small and Milesi, 2013).

As discussed by (Holden and Woodcock, 2016), differences in the OLI and ETM+ spectral responses have implications for comparability of spectral indices. Vegetation indices are a class of commonly used spectral indices with a direct relationship to one of the land cover fractions (i.e. vegetation fraction). While the relationship between indices for Landsat ETM+ has already been shown (Small and Milesi, 2013), this relationship may change on the global scale for OLI due to changes in NIR band positioning resulting in small changes in the intensity of the red edge. To illustrate the new relationship for OLI and the new global

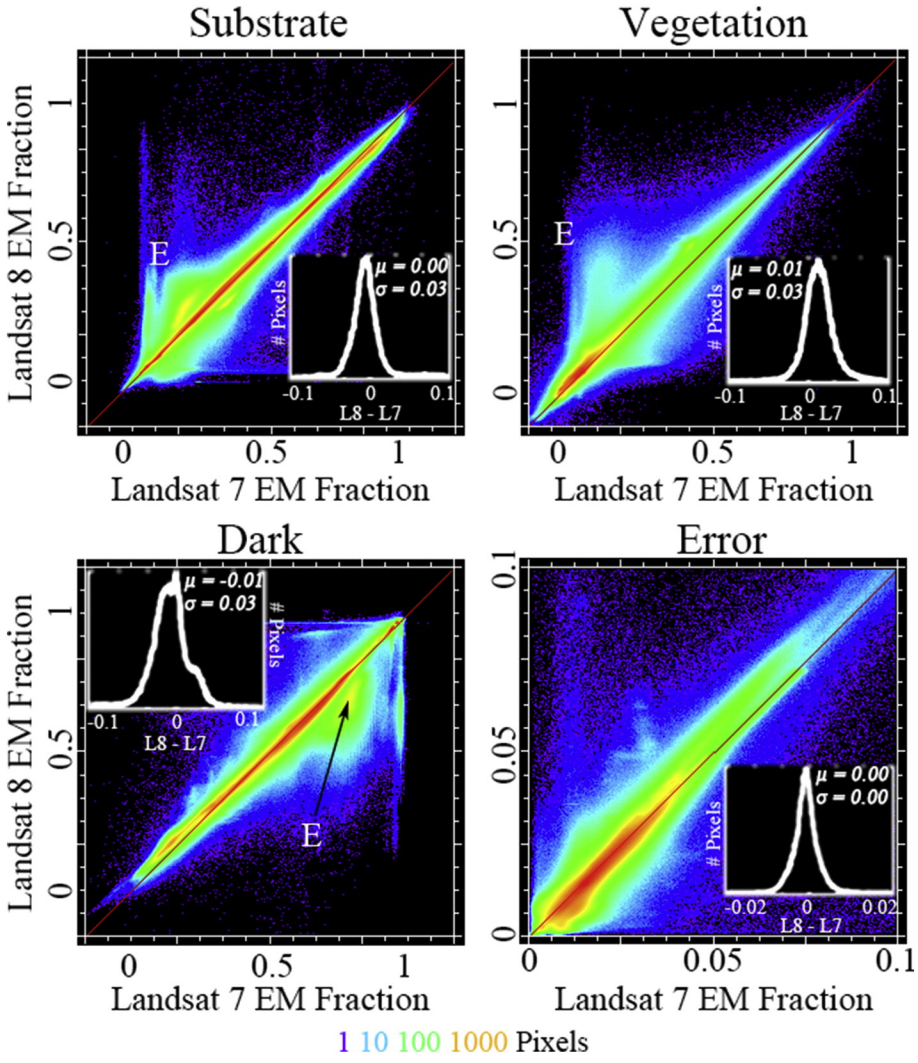

Fig. 6. Intercomparison of SVD fractions derived from 80,910,343 near-simultaneous ETM+ and OLI spectra using the new underflight ETM+ and OLI EMs. All fractions (including error) show minimal bias (μ ≤ 1%) off the 1:1 line. Scatter corresponds to either pixels with changing atmosphere in the 1–6 min between satellite overpasses or subpixel displacements between images. Evaporites (E) are not well represented by the SVD model so they also plot off axis. Inset histograms show fraction difference distributions. All three SVD fractions show >95% of all pixels with differences in the range ± 5%. Error differences show 98% of all pixels have <1% change across sensors for the SVD model.

EMs from this study, we compare three commonly used vegetation indices with vegetation fraction estimates for the diversity of Landsat 8 OLI spectra in the underflight collection. Fig. 7 shows the relation between subpixel vegetation fraction (Fv) as estimated with the new global SVD EMs and three commonly used vegetation indices: Normalized Difference Vegetation Index (NDVI, (Rouse et al., 1973)), Enhanced Vegetation Index (EVI, (Huete et al., 2002)), and Soil Adjusted Vegetation Index (SAVI, (Huete, 1988)).

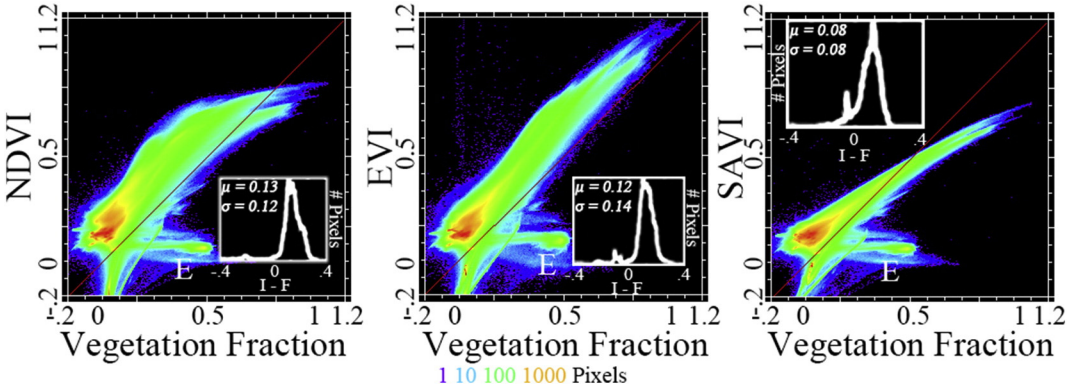

Fig. 7. Vegetation index intercomparison. NDVI, EVI, and SAVI relative to vegetation fraction of the same 80,910,343 OLI spectra. SAVI and EVI are quasi-linear functions of vegetation fraction, but with varying dispersion and slope. NDVI shows nonlinear saturation above 0.5 with considerable dispersion at all fractions.

The equation used for NDVI is:

$$\frac{\mathrm{NIR}-V_r}{\mathrm{NIR}+V_r}$$

The equation used for EVI is:

$$2.5 * \frac{\mathrm{NIR}-V_r}{\mathrm{NIR}+6*V_r-7.5*V_b+1}$$

The equation used for SAVI is:

$$1.5 * \frac{\mathrm{NIR}-V_r}{\mathrm{NIR}+V_r+0.5}$$

The relationship between SAVI and Fv is relatively linear for most pixels with Fv > 0.2, although a substantial bias is present and variance is wide at low values. The relationship between EVI and Fv is also linear, although with considerable variability and positive offset from the 1:1 line. The relationship between NDVI and Fv is substantially more complex and shows the well-known saturation effect at high vegetation fractions.

5. Discussion

The complex relationships of the vegetation indices shown in Fig. 7 may not be intuitive given their arithmetic simplicity. This complexity is not a function of the geographic limitation of the study or of the limitations of SMA. Instead, the complexity can be shown to have a simple physical explanation.

To illustrate the basis for the complexity of these relations, we simulate the effects of subpixel soil reflectance, shadow and atmospheric scattering on these vegetation indices, compared to true vegetation fraction. Consider a hypothetical 30 × 30 m Landsat pixel filled with some amount of green vegetation and some amount of exposed soil and some amount of shadow. Based on the solar geometry illuminating the pixel, there will be some variable amount of area (viewed from directly above) of subpixel shadow cast by the roughness of the soil and the height and geometry of the vegetation. Areas in deep shadow are illuminated only by diffuse scattering with a spectrum dominated by Rayleigh scattering in the atmospheric column between the ground and sensor – as illustrated by the Dark EM. Between deep shadow and illuminated substrate and vegetation is a continuous triangular plane of spectral mixtures. This plane includes 100% illuminated vegetation with no soil or shadow, 100% illuminated soil with no vegetation or shadow, and 100% deep shadow (Rayleigh scattering only) – as well as all combinations thereof. In the case of single scattering, the sensor essentially integrates these continuous endmember spectra as a linear sum into a single 6-element broadband spectrum. We use the atmospherically corrected LEDAPS surface reflectance EMs from (Small and Milesi, 2013) with the linear spectral mixture model to simulate all possible integer mixtures of substrate, vegetation and shadow, then compute vegetation indices (NDVI and EVI) for each synthetic mixture.

Fig. 8 shows the results of a Monte Carlo simulation for every possible mixture of vegetation, soil and shadow in 1% increments, resulting in 5050 simulated Landsat spectra. This simulation is run for 3 different levels of atmospheric "noise" (in the form of adding an increasingly opaque Rayleigh scattering spectrum as the dark EM) based on the expected analytical relationship between scattering of light by particles much smaller than the wavelength ($r \propto \lambda^{-4}$). The simulation is also run for 3 different background soils (produced by varying the amplitude of the soil spectrum as the substrate EM). A common vegetation spectrum was used for all runs and was chosen to represent a sample broadband spectrum of healthy photosynthetic vegetation.

Fv, NDVI and EVI are then computed for all of these synthetic mixtures. As expected, inversion of the linear SVD model yields accurate results for Fv, with minimal bias and scatter (in all cases $\mu < 0.5\%$ and maximum error of any pixel <2.5%), with nearly uniform dispersion across the full range of values. The correlation between "true" input fractional vegetative cover and Fv estimated by unmixing using SMA in this model is 0.9999.

However, the behavior of the vegetation indices is more complex. Varying the amplitude of atmospheric noise or the spectrum of the soil substrate can substantially alter the bias and curvature of the indices. Over a wide range of soils, EVI exhibits substantial linearity with Fv, although it consistently plots above the 1:1 line for all but the brightest soil. EVI is also shown to deviate more strongly from linearity with more severe atmosphere, especially at high vegetation fractions. NDVI demonstrates its well-known

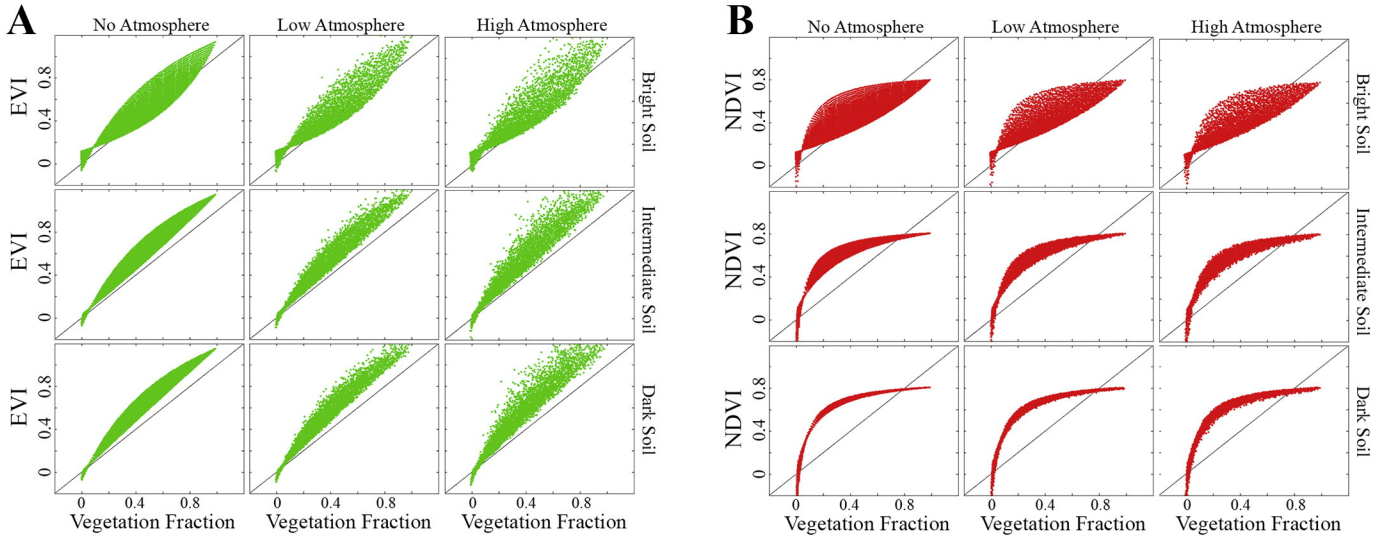

Fig. 8. a. Calculation of EVI for synthetic mixtures containing every possible integer combination of subpixel soil, vegetation, and shadow. EVI exhibits more linearity over a wider range than NDVI. High values of EVI show sensitivity to atmospheric perturbations. b. Calculation of NDVI for synthetic mixtures containing every possible integer combination of subpixel soil, vegetation, and shadow. Slight variations in the amount of atmospheric perturbation (simulated as Rayleigh scatter times a small random number) and brightness of the soil substrate can yield substantial differences in the value of the index.

saturation at high values and greatly variable nonlinear dependency on the soil spectrum.

This range of values for spectral indices with small variations in atmospheric and soil parameters is a result of the functional form of the equations used in the computation of the indices. NDVI is a simple ratio of the sum and difference of 2 bands. EVI introduces the visible blue band in order to account for atmospheric variability, and exhibits substantially enhanced stability over a range of conditions as a result. Fv uses the full information content of all 6 bands in the spectrum and explicitly accounts for the contributions of both soil and shadow. This results in enhanced theoretical stability of fraction estimates over indices based on only 2 or 3 bands – stability which also applies to any systematic perturbations which affect all pixels equally that may be introduced by the changes in spectral response between ETM+ and OLI.

To the extent that the perturbations affect the EMs in the same way they would affect any other pixel, selection of new EMs will adjust the model and correct the subpixel fraction estimates accordingly. This illustrates two fundamental strengths of the linear mixture model relative to indices that use a subset of bands and do not account for other factors contributing to the mixed pixel reflectance. The use of standardized global endmembers extends these benefits by making fraction estimates intercomparable across time and space. We note that the availability of standardized global endmembers in no way reduces the utility of locally derived, application-specific endmembers. Given the ease with which fraction estimates are obtained, analyses can easily include fractions from both local and global endmembers for comparison. In fact, given the spectral diversity of the plane of substrates, we advocate the use of local substrate endmembers which may often be more suitable for substrate-oriented analyses than the very bright substrate endmember given here.

Importantly, we also note that this stability also only extends to systematic perturbations which propagate into the EMs. For instance, linear mixture models are not able to correct for perturbations to the reflectance spectrum produced by spatially and temporally localized atmospheric variability. The global linear mixture model presented here, and indeed no linear mixture model at all, can fully resolve most atmospheric effects – or any similar effects which are not systematic perturbations to the spectral mixing space. This is particularly the case when the effects are nonlinear.

6. Conclusions

Subpixel EM fractions for Landsats 7 and 8 imaged in underflight configuration over a wide range of land cover show considerable agreement and can be well-characterized by the simple 1:1 relation with minimal bias or scatter. RMS misfit for both sensors using these new models remains <5% for >98% of the >80 million pixels, as good or better than the previous EMs. It is also notable that no atmospheric correction was attempted for this study (beyond the selection of subscenes which appeared to be cloud-free). The increasing availability of standardized surface reflectance products should only improve upon this result. The agreement found in this study is testament to the work done by those at NASA, the USGS, and all those who are responsible for the design and implementation of the radiometric cross-calibration of these sensors.

The results of the EM fraction comparison suggest that the differences in bandpasses between the two sensors can effectively be taken into account by the use of new EMs based on the near-simultaneous imaging of the same geographical locations by the two sensors – with no additional radiometric correction. In addition, these EMs now more fully span the global mixing space than previous EMs due to the inclusion of additional bright sands which extend the plane of substrates beyond previous studies. We suggest that these new global EMs supplant the EMs from previous studies. These EMs are freely available online at: www.LDEO.columbia.edu/~small/GlobalLandsat/ and are included here as Supplementary Materials in plain text format.

However, the behavior of spectral indices, as already noted by others, is substantially more complex and may require cross-calibration beyond direct download of L1T imagery from the USGS archive if such indices are to be used operationally to compare TM/ETM+ and OLI imagery, as discussed by (Holden and Woodcock, 2016) and (Roy et al., 2016).

Acknowledgements

The authors thank those responsible for the free availability of the Landsat imagery used in this study, as well as those responsible for the extensive preprocessing of that imagery to facilitate its use. The authors thank three anonymous reviewers, especially Reviewer #3, for comments and suggestions which improved the clarity of the manuscript. Work done by D. Sousa was conducted with Government support under FA9550-11-C-0028 and awarded by the Department of Defense, Air Force Office of Scientific Research, National Defense Science and Engineering Graduate (NDSEG) Fellowship, 32 CFR 168a. CS was funded by the NASA MultiSource Land Imaging Program (grant NNX15AT65G). D. Sousa thanks M.B. Sousa for a lifetime of helpful and clarifying conversations.

Appendix A. Supplementary data

Supplementary data to this article can be found online at http://dx.doi.org/10.1016/j.rse.2017.01.033.

References

Adams, J.B., Smith, M.O., Johnson, P.E., 1986. Spectral mixture modeling: a new analysis of rock and soil types at the Viking Lander 1 site. J. Geophys. Res. Solid Earth 91, 8098–8112 (1978–2012).

Boardman, J.W., 1993. Automating spectral unmixing of AVIRIS data using convex geometry concepts. Summaries of the 4th Annual JPL Airborne Geoscience Workshop. Volume 1: AVIRIS Workshop. JPL, pp. 11–14.

Chander, G., Markham, B., 2003. Revised Landsat-5 TM radiometric calibration procedures and postcalibration dynamic ranges. IEEE Trans. Geosci. Remote Sens. 41, 2674–2677.

Flood, N., 2014. Continuity of reflectance data between Landsat-7 ETM+ and Landsat-8 OLI, for both top-of-atmosphere and surface reflectance: a study in the Australian landscape. Remote Sens. 6, 7952–7970.

Holden, C.E., Woodcock, C.E., 2016. An analysis of Landsat 7 and Landsat 8 underflight data and the implications for time series investigations. Remote Sens. Environ. 185, 16–36.

Huete, A.R., 1988. A soil-adjusted vegetation index (SAVI). Remote Sens. Environ. 25, 295–309.

Huete, A., Didan, K., Miura, T., Rodriguez, E.P., Gao, X., Ferreira, L.G., 2002. Overview of the radiometric and biophysical performance of the MODIS vegetation indices. Remote Sens. Environ. 83, 195–213.

Knight, J.E., Kvaran, G., 2014. Landsat-8 Operational Land Imager design, characterization and performance. Remote Sens. 6.

Markham, B.L., Helder, D.L., 2012. Forty-year calibrated record of earth-reflected radiance from Landsat: a review. Remote Sens. Environ. 122, 30–40.

Mishra, N., Helder, D., Barsi, J., Markham, B., 2016. Continuous calibration improvement in solar reflective bands: Landsat 5 through Landsat 8. Remote Sens. Environ. 185, 7–15.

Morfitt, R., Barsi, J., Levy, R., Markham, B., Micijevic, E., Ong, L., Scaramuzza, P., Vanderwerff, K., 2015. Landsat-8 Operational Land Imager (OLI) radiometric performance on-orbit. Remote Sens. 7.

Olson, D.M., Dinerstein, E., Wikramanayake, E.D., Burgess, N.D., Powell, G.V.N., Underwood, E.C., D'Amico, J.A., Itoua, I., Strand, H.E., Morrison, J.C., Loucks, C.J., Allnutt, T.F., Ricketts, T.H., Kura, Y., Lamoreux, J.F., Wettengel, W.W., Hedao, P., Kassem, K.R., 2001. Terrestrial ecoregions of the world: a new map of life on earth: a new global map of terrestrial ecoregions provides an innovative tool for conserving biodiversity. Bioscience 51, 933–938.

Rouse, J.W., Haas, R.H., Schell, J.A., Deering, D.W., 1973. Monitoring vegetation systems in the Great Plains with ERTS. Third ERTS Symposium. NASA, pp. 309–317.

Roy, D.P., Kovalskyy, V., Zhang, H.K., Vermote, E.F., Yan, L., Kumar, S.S., Egorov, A., 2016. Characterization of Landsat-7 to Landsat-8 reflective wavelength and normalized difference vegetation index continuity. Remote Sens. Environ. 185, 57–70.

Schott, J.R., Gerace, A., Woodcock, C.E., Wang, S., Zhu, Z., Wynne, R.H., Blinn, C.E., 2016. The impact of improved signal-to-noise ratios on algorithm performance: case studies for Landsat class instruments. Remote Sens. Environ. 185, 37–45.

Singer, R.B., McCord, T.B., 1979. Mars-Large scale mixing of bright and dark surface materials and implications for analysis of spectral reflectance. Lunar and Planetary Science Conference Proceedings, pp. 1835–1848.

Small, C., 2004. The Landsat ETM+ spectral mixing space. Remote Sens. Environ. 93, 1–17.

Small, C., Milesi, C., 2013. Multi-scale standardized spectral mixture models. Remote Sens. Environ. 136, 442–454.
Storey, J., Choate, M., Lee, K., 2014. Landsat 8 operational land imager on-orbit geometric calibration and performance. Remote Sens. 6.
USGS, 2016. Provisional LaSRC Product Guide, Version 3.3. http://landsat.usgs.gov/documents/provisional_lasrc_product_guide.pdf.
Vogelmann, J.E., Gallant, A.L., Shi, H., Zhu, Z., 2016. Perspectives on monitoring gradual change across the continuity of Landsat sensors using time-series data. Remote Sens. Environ. 185, 258–270.
Wulder, M.A., White, J.C., Loveland, T.R., Woodcock, C.E., Belward, A.S., Cohen, W.B., Fosnight, E.A., Shaw, J., Masek, J.G., Roy, D.P., 2016. The global Landsat archive: status, consolidation, and direction. Remote Sens. Environ. 185, 271–283.